

# Unlocking the High Rate Performance of $\text{Na}_{0.44}\text{MnO}_2$ with a Boron Doping Strategy

Wenchong Ding, Zhongqiang Ye, Zhifeng Huang, Hai Hu,\* and Li Liu\*

As the cathode material of sodium-ion battery, sodium manganese oxide has attracted considerable critical attention due to its abundant resources and low cost. However, due to the disproportionation of manganese, sodium manganese oxide often suffers from significant capacity degradation and low rate performance, which hinders its practical application. Here, the electrochemical performance of  $\text{Na}_{0.44}\text{MnO}_2$  is significantly improved by an appropriate

amount of B doping. The  $\text{Na}_{0.44}\text{Mn}_{0.95}\text{B}_{0.05}\text{O}_2$  shows outstanding rate capability and excellent cycle performance, which could deliver a capacity of  $61.0 \text{ mAh g}^{-1}$  at  $60 \text{ C}$  and a capacity retention of 84.7% for 400 cycles at  $30 \text{ C}$ . B doping could effectively improve the electronic/ionic conductivity of  $\text{Na}_{0.44}\text{MnO}_2$ , which has been demonstrated.

## 1. Introduction

Since the early 1990s, the global energy crisis has emerged as a critical issue, prompting an increased focus on finding sustainable solutions. The urgency to protect the environment has accelerated the development of clean and sustainable energy sources, consequently driving advancements in energy storage devices.<sup>[1,2]</sup> The push for higher efficiency, spurred by advancements in personal computers, electronics, telecommunications, and semiconductor technologies, has escalated significantly. The wave of the energy crisis and the resulting regulatory requirements have made efficiency a more crucial attribute of power systems, particularly concerning energy conservation and total cost of ownership. Additionally, with the proliferation of electric vehicles, the lower power density of batteries has become a barrier to achieving high-speed vehicle operation, highlighting the urgent need to improve the efficiency of portable energy devices. Power density, defined as the maximum output power per unit mass of the battery, depends significantly on the capacity of electrode materials to deliver energy under high-density currents, which is essential for enhancing the power density of batteries.<sup>[3]</sup> Lithium-ion batteries (LIBs), due to their portability, high theoretical energy density ( $200\text{--}350 \text{ Wh kg}^{-1}$  for NCM,  $150\text{--}210 \text{ Wh kg}^{-1}$  for LFP), and extended cycle life, have become ubiquitous in 3 C electronics, electric vehicles, and other applications.<sup>[4]</sup> However, the limited and unevenly allocated lithium resources result in high costs, rendering lithium-ion batteries less ideal for large-scale energy storage systems. In response, sodium-ion batteries (SIBs) have gained increasing attention as a promising alternative. They

offer a similar working principle, lower cost, and higher safety, though their theoretical energy density ( $70\text{--}200 \text{ Wh kg}^{-1}$ ) is not as high as that of lithium-ion batteries.<sup>[5]</sup> This article focuses on enhancing the performance of sodium-ion batteries under high-density currents.

Previous studies have synthesized various cathode materials with suitable structures, such as polyanionic phosphates, Prussian blue analogs, layered oxides ( $\text{Na}_x\text{MnO}_2$ ,  $0.44 < x \leq 1$ ), and tunnel-type oxides ( $\text{Na}_{0.44}\text{MnO}_2$ ).<sup>[6]</sup> Tunnel-type oxides, especially, have attracted considerable interest due to their exceptional stability and distinctive framework structure. The tunnel-type structure shown in Figure S1 (Supporting Information), characterized by its unique 3D architecture featuring edge-sharing  $\text{MnO}_6$  and corner-sharing  $\text{MnO}_5$  polyhedrons, presents an intriguing design. In the tunnel structure,  $\text{Na}^+$  diffuses along the c-axis and occupies three different sites. The Na1 site, located in a pentagonal tunnel, is fully occupied, presenting a high diffusion barrier that makes the extraction of  $\text{Na}^+$  nearly impossible.  $\text{Na}^+$  at the Na3 site is subject to electrostatic repulsion from Na2, adjacent Na3 ions, and surrounding tunnels. This results in only 50% occupancy of the S-type tunnel when the material is fresh.<sup>[7]</sup> These factors contribute to the lower initial capacity performance of the tunnel-type structure and also explain the slight increase in capacity observed in tunnel-type cathodes during long-term cycling. Additionally, the electrochemical performance is hindered by the severe disproportionation of  $\text{Mn}^{3+}$  into  $\text{Mn}^{2+}$  and  $\text{Mn}^{4+}$  during sodiation/desodiation processes.<sup>[8]</sup>

To overcome the challenges associated with Mn-based tunnel cathode materials and enhance their electrochemical properties, various strategies have been explored. For instance, doping with anions or cations to reduce the dissolution of  $\text{Mn}^{3+}$ , thereby enhancing structural stability. Zhan et al. discovered that partially substituting Mn with Ti to prepare  $\text{Na}_{0.44}\text{Mn}_{0.78}\text{Ti}_{0.22}\text{O}_2$  could maintain the tunnel structure and improve the cycling stability of the  $\text{Na}_{0.44}\text{MnO}_2$  cathode material at  $100 \text{ mA g}^{-1}$ . The presence of inactive Ti during the charge-discharge cycle lowered the discharge specific capacity of the cathode material, although it enhanced the rate performance at different current densities.

W. Ding, Z. Ye, Z. Huang, H. Hu, L. Liu  
School of Chemistry  
Xiangtan University  
Xiangtan 411105, China  
E-mail: [huhai@xtu.edu.cn](mailto:huhai@xtu.edu.cn)  
[liuli@xtu.edu.cn](mailto:liuli@xtu.edu.cn)

 Supporting information for this article is available on the WWW under <https://doi.org/10.1002/batt.202500029>

Specifically, at  $100 \text{ mAg}^{-1}$ , the discharge specific capacity was  $60 \text{ mAhg}^{-1}$ , which is 55% of the capacity at  $20 \text{ mAg}^{-1}$ .<sup>[9]</sup> Several studies have focused on improving the rate performance of tunnel-type cathode materials. For example, Li et al. employed a Mg doping strategy to synthesize  $\text{Na}_{0.44}\text{Mn}_{0.95}\text{Mg}_{0.05}\text{O}_2$ . The addition of Mg significantly enhanced the rate performance, allowing the cathode material to deliver a capacity of  $60 \text{ mAh g}^{-1}$  at  $30 \text{ C}$ , which is 57% of its capacity at  $0.2 \text{ C}$ . Furthermore, the material demonstrated excellent cycling stability, maintaining 67% of its capacity after 800 cycles at  $2 \text{ C}$ .<sup>[10]</sup> Modification strategies for other types of sodium-ion battery cathode materials also offer valuable insights. For instance, in the case of polyanion-type manganese-based cathodes, Liu et al. employed an electrostatic spray method to synthesize  $\text{Na}_2\text{Fe}_5(\text{SO}_4)_9@\text{rGO}$ . The introduction of a reduced graphene oxide (rGO) coating significantly enhanced the initial discharge capacity from 59 to  $100 \text{ mAh g}^{-1}$  at  $0.2 \text{ C}$ . Moreover, the material demonstrated excellent rate capability, delivering a capacity of  $63 \text{ mAh g}^{-1}$  at a high current density of  $50 \text{ C}$ .<sup>[11]</sup> Similarly, Guan et al. synthesized rGO-coated  $\text{Na}_3\text{V}_2(\text{PO}_4)_2\text{F}_3$  nanocuboids via a microwave-assisted hydrothermal method. Compared to pristine  $\text{Na}_3\text{V}_2(\text{PO}_4)_2\text{F}_3$ , the rGO-coated material exhibited a substantial improvement in capacity retention at  $50 \text{ C}$ , indicating a remarkable enhancement in rate performance.<sup>[12]</sup> These strategic advancements underscore the potential for tailored approaches to address the limitations of Mn-based tunnel cathode materials, offering promising prospects for advancements in energy storage technologies.

Herein, inspired by these effective modification strategies, B-doped  $\text{Na}_{0.44}\text{MnO}_2$  materials have been synthesized by a citric acid-assisted sol-gel method, the electrochemical performance of B-doped  $\text{Na}_{0.44}\text{MnO}_2$  was systematically investigated in both half-cell and full-cell configurations to evaluate its practical applicability. It is found that appropriate amount of B doping could effectively improves the electronic/ionic conductivity, thus  $\text{Na}_{0.44}\text{Mn}_{0.95}\text{B}_{0.05}\text{O}_2$  shows significantly improved electrochemical performance than pristine  $\text{Na}_{0.44}\text{MnO}_2$ , especially the rate capability.

## 2. Results

A series of B-doped  $\text{Na}_{0.44}\text{MnO}_2$  nanorods were synthesized using the sol-gel method. **Figure 1a** displays the X-ray diffraction (XRD) patterns of  $\text{Na}_{0.44}\text{MnO}_2$  and  $\text{Na}_{0.44}\text{Mn}_{0.95}\text{B}_{0.05}\text{O}_2$ . Most peaks of both samples correspond well with the standard card for  $\text{Na}_4\text{Mn}_9\text{O}_{18}$  (PDF#27-0750) with the Pbam orthorhombic structure. After B substitution,  $\text{Na}_{0.44}\text{Mn}_{0.95}\text{B}_{0.05}\text{O}_2$  shows impurity peaks at  $23.12^\circ$ ,  $32.92^\circ$ ,  $38.20^\circ$ ,  $49.32^\circ$ , and  $55.14^\circ$  match the standard card of  $\text{Mn}_2\text{O}_3$  (PDF#24-0508). Other B-doped samples also show similar impurity phase of  $\text{Mn}_2\text{O}_3$  (Figure S2, Supporting Information), and the intensity of the impure phase increases monotonically with higher B doping levels. It is demonstrated that B doping induces the decomposition of  $\text{Na}_{0.44}\text{MnO}_2$  into the  $\alpha\text{-Mn}_2\text{O}_3$  phase, but according to literature reports, the  $\alpha\text{-Mn}_2\text{O}_3$  phase remains stable during charge-discharge cycles and does not affect cycling performance.<sup>[13]</sup> In the XRD pattern of  $\text{Na}_{0.44}\text{MnO}_2$ , impurity peaks at  $12.56^\circ$  and  $13.40^\circ$  match todorokite  $\text{NaMn}_6\text{O}_{12}\cdot3\text{H}_2\text{O}$ , a hydrated sodium manganese oxide. This phase forms due to the reaction of manganese oxide with water when the calcined material is exposed to air. Notably, the B-doped material does not show this hydrated phase, indicating that B doping improves the air stability of  $\text{Na}_{0.44}\text{MnO}_2$ . Figure 1b and Figure S2 (Supporting Information) present the Rietveld refinement results of  $\text{Na}_{0.44}\text{Mn}_{0.95}\text{B}_{0.05}\text{O}_2$  and  $\text{Na}_{0.44}\text{MnO}_2$  obtained using GSAS II (a software for determination of crystal structures and diffraction-based materials characterization for crystalline solids on all scales), with the corresponding lattice parameters provided in Table S1–S3 (Supporting Information). The introduction of B causes slight lattice expansion in  $\text{Na}_{0.44}\text{MnO}_2$ . Specifically,  $\text{Na}_{0.44}\text{MnO}_2$  has lattice parameters of  $a = 9.0875 \text{ \AA}$ ,  $b = 26.4428 \text{ \AA}$ , and  $c = 2.8245 \text{ \AA}$ , while  $\text{Na}_{0.44}\text{Mn}_{0.95}\text{B}_{0.05}\text{O}_2$  has  $a = 9.1143 \text{ \AA}$ ,  $b = 26.4113 \text{ \AA}$ , and  $c = 2.8301 \text{ \AA}$ . The increase in the values of  $a$  and  $c$ , along with the slight decrease in  $b$ , confirms the successful incorporation of B into the TM layer. The expansion of the parameters  $a$  and  $c$  facilitates the diffusion of  $\text{Na}^+$  ions within the tunnel structure.<sup>[14]</sup> The unit cell volume expands from

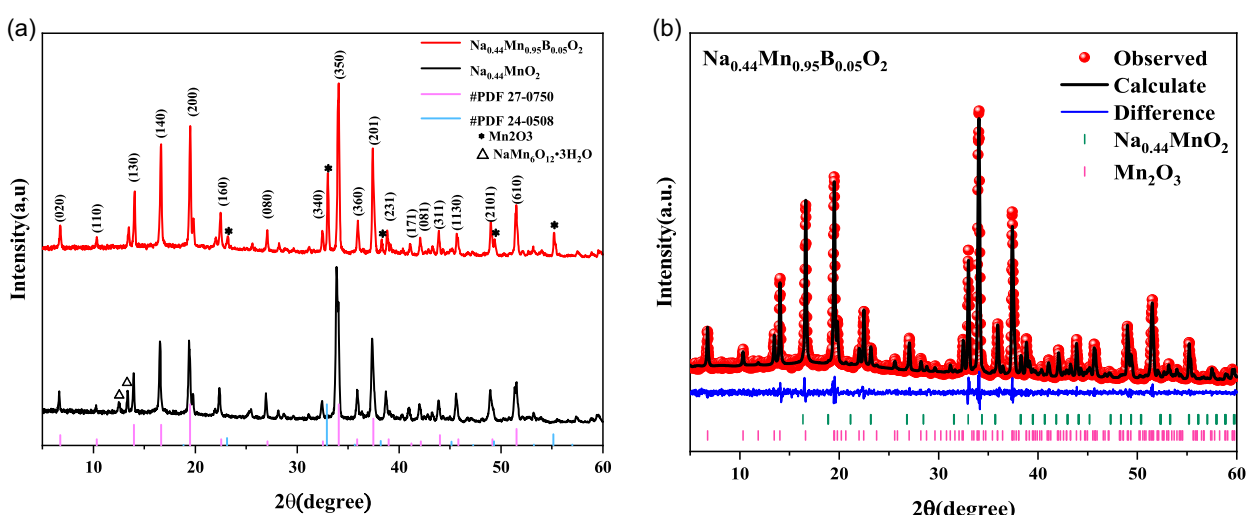


**Figure 1.** a) XRD patterns of  $\text{Na}_{0.44}\text{MnO}_2$  and  $\text{Na}_{0.44}\text{Mn}_{0.95}\text{B}_{0.05}\text{O}_2$ . b) Rietveld refinement results of  $\text{Na}_{0.44}\text{Mn}_{0.95}\text{B}_{0.05}\text{O}_2$ .

$678.73\text{ \AA}^3$  for  $\text{Na}_{0.44}\text{MnO}_2$  to  $681.27\text{ \AA}^3$  for  $\text{Na}_{0.44}\text{Mn}_{0.95}\text{B}_{0.05}\text{O}_2$ . B incorporation effectively increases the Na—O bond length and decreases the TM—O bond length, thereby expanding the unit cell volume.<sup>[15]</sup> Additionally, the bond energy of B—O ( $\Delta H_f$  (298 K) = 809 kJ mol<sup>-1</sup>) is higher than that of Mn—O ( $\Delta H_f$  (298 K) = 402 kJ mol<sup>-1</sup>). The stronger bond energy enhances structural stability. Expanding crystal cells will provide greater space for Na ion intercalation/deintercalation, which is beneficial for electrochemical reaction kinetics. Furthermore, B exhibits a strong electronegativity and is prone to form compounds such as  $(\text{BO}_4)^{5-}$ . Based on the refinement results (Table S3, Supporting Information), it can be inferred that B tends to substitute the  $\text{Mn}^{3+}$  ions and occupy the octahedral sites (Mn2) in the  $\text{MnO}_6$  framework.

Figure 2a,b shows the SEM images of  $\text{Na}_{0.44}\text{MnO}_2$  and  $\text{Na}_{0.44}\text{Mn}_{0.95}\text{B}_{0.05}\text{O}_2$ . Both samples show submicron rods with grooves, with diameters ranging from 220 to 380 nm. For  $\text{Na}_{0.44}\text{MnO}_2$ , growth along the (001) direction typically results in fewer crystal defects and internal stresses, suggesting that the surface energy in this direction is minimized, leading to more stable crystal growth and the formation of a rod-like morphology. Furthermore, it has been reported that Na, acting as a flux agent, facilitates rapid ion diffusion due to its high mobility, thereby playing a pivotal role in the rod-like growth process.<sup>[16]</sup> The introduction of B does not exert a notable influence on the morphology of the tunnel-type material. To clarify the impact of doping on the crystal structure, high-resolution transmission electron microscopy (HRTEM) characterization was conducted on both materials. As shown in Figure 2c,d, HRTEM images reveal clear lattice fringes of (2 0 0) crystal plane, and the spacing of the lattice fringe for  $\text{Na}_{0.44}\text{Mn}_{0.95}\text{B}_{0.05}\text{O}_2$  is 4.612 Å, which is larger than that of  $\text{Na}_{0.44}\text{MnO}_2$  (4.607 Å). This result is consistent with the XRD results.<sup>[17]</sup> EDS mapping images in Figure 2e demonstrate the uniform distribution of Na, Mn, and B, indicating successful doping of B into  $\text{Na}_{0.44}\text{Mn}_{0.95}\text{B}_{0.05}\text{O}_2$ .

The Fourier-transform infrared spectroscopy (FTIR) spectra of  $\text{Na}_{0.44}\text{Mn}_{1-x}\text{B}_x\text{O}_2$  ( $x = 0, 0.05, 0.1$ , and  $0.2$ ) are shown in Figure S4 (Supporting Information). It shows that an increase in the intensity of the characteristic peak of  $(\text{BO}_4)^{5-}$  at  $955\text{ cm}^{-1}$  can be observed with the increase of B amount.

This demonstrates that B exists in the structure of  $\text{Na}_{0.44}\text{MnO}_2$  as  $(\text{BO}_4)^{5-}$  tetrahedra.

To investigate the effect of B doping on the chemical states of elements, XPS tests were conducted on  $\text{Na}_{0.44}\text{MnO}_2$  and  $\text{Na}_{0.44}\text{Mn}_{0.95}\text{B}_{0.05}\text{O}_2$ . As shown in the spectra (Figure 3a), the presence of Na, Mn, O, and B in  $\text{Na}_{0.44}\text{Mn}_{0.95}\text{B}_{0.05}\text{O}_2$  is confirmed, and further analysis of the high-resolution spectra of each element is performed. In the Mn2p signal (Figure 3b), two broad peaks at 641.73 and 652.39 eV are observed, corresponding to  $\text{Mn}2\text{p}^{3/2}$  and  $\text{Mn}2\text{p}^{1/2}$ , indicating the presence of Mn in  $\text{Na}_{0.44}\text{MnO}_2$  and  $\text{Na}_{0.44}\text{Mn}_{0.95}\text{B}_{0.05}\text{O}_2$  exists in the forms of  $\text{Mn}^{3+}$  and  $\text{Mn}^{4+}$ . Specifically, the binding energy peaks at 640.87 and 652.25 eV are assigned to  $\text{Mn}^{4+}$ , whereas those at 642.12 and 653.37 eV correspond to  $\text{Mn}^{3+}$ .<sup>[18]</sup> The area ratio of  $\text{SMn}^{4+}/\text{SMn}^{3+}$  is 0.99 for  $\text{Na}_{0.44}\text{MnO}_2$  and 1.12 for  $\text{Na}_{0.44}\text{Mn}_{0.95}\text{B}_{0.05}\text{O}_2$ , showing a slight reduction in  $\text{Mn}^{3+}$  due to the addition of B. In the O1s spectrum (Figure 3c), the peaks at 529.44, 531.07, and 533.03 eV correspond to lattice oxygen, oxygen vacancies, and surface oxygen, respectively. For  $\text{Na}_{0.44}\text{Mn}_{0.95}\text{B}_{0.05}\text{O}_2$ , the peak area representing oxygen vacancies at 537.01 eV is significantly larger compared to the oxygen vacancy peak area in  $\text{Na}_{0.44}\text{MnO}_2$ , indicating a substantial increase in oxygen vacancies. According to Jiang et al. oxygen vacancies can enhance the electron transfer rate within the structure, and improving conductivity.<sup>[19]</sup> For tunnel-type  ${}^{0.44}\text{MnO}^2$ , the formation energy of oxygen vacancies is relatively low, which allows for the generation of oxygen vacancies under appropriate pressure and temperature conditions.<sup>[20]</sup> Due to the considerable difference in ionic radius between  $\text{B}^{3+}$  and  $\text{Mn}^{3+}/\text{Mn}^{4+}$ , the tetrahedral  $(\text{BO}_4)^{5-}$  units preferentially replace  $\text{Mn}(\text{III})\text{O}_6$ .<sup>[13]</sup> Additionally, a fraction of B atoms incorporates into the interstitial sites within the transition metal oxide layers, inducing lattice distortion. This structural perturbation facilitates the migration of oxygen atoms, resulting in an increased concentration of oxygen vacancies. Previous studies by Chu et al. demonstrated that B doping in  $\text{MnO}^2$  effectively introduces additional oxygen vacancies, which were further substantiated through X-ray photoelectron spectroscopy (XPS) and Raman spectroscopy.<sup>[17]</sup> Raman spectroscopy, in particular, serves as a valuable tool for detecting oxygen vacancies.<sup>[21]</sup> As illustrated in Figure S5 (Supporting Information), the Raman spectra of  ${}^{0.44}\text{MnO}^2$  and

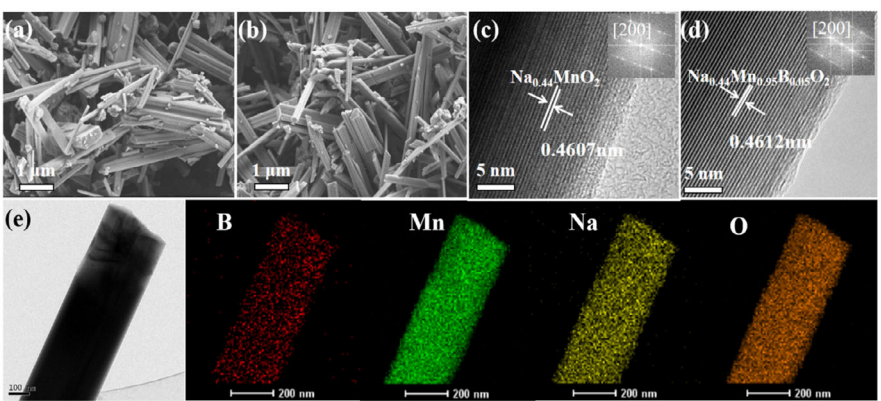
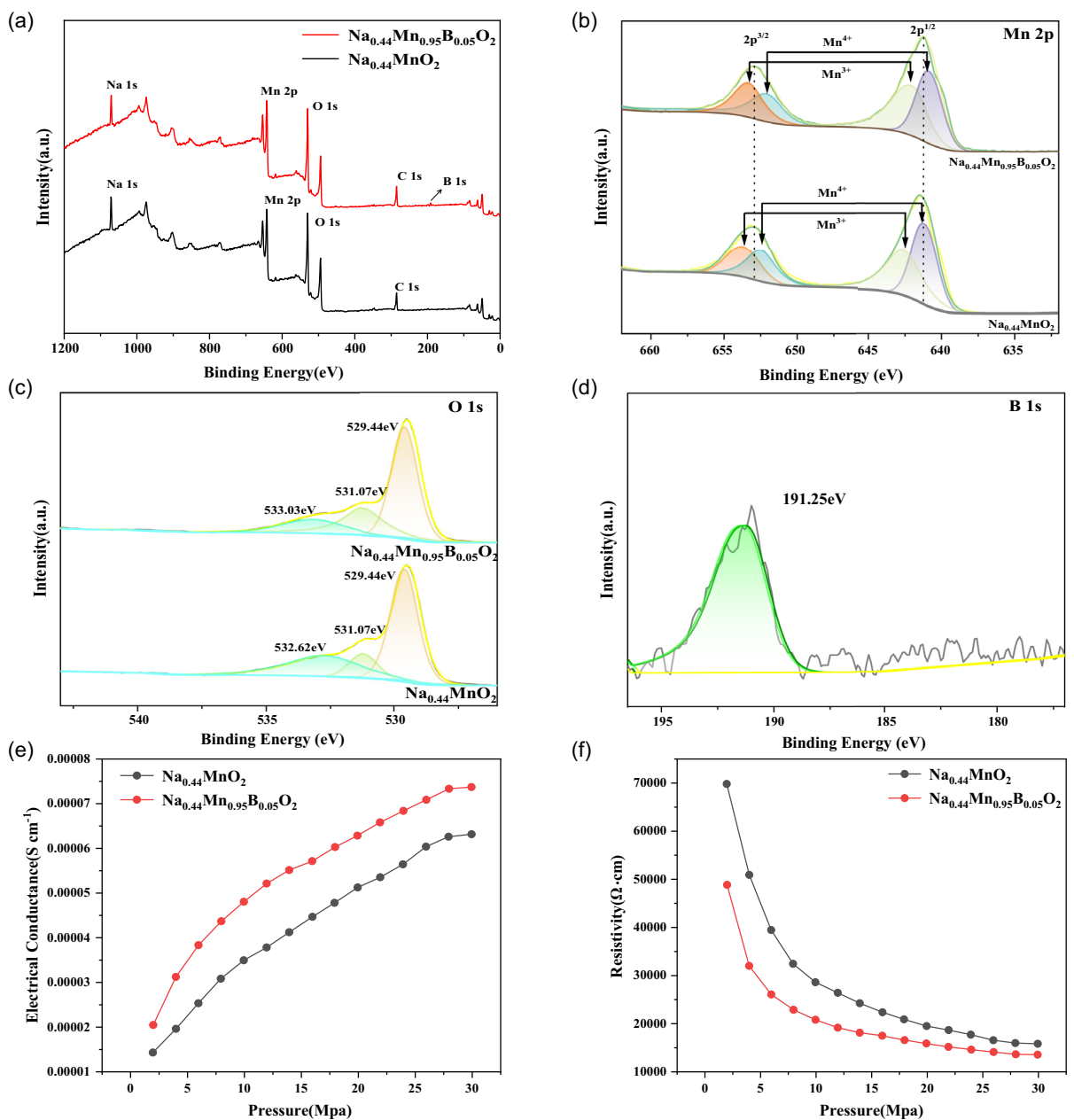


Figure 2. SEM micrographs for a)  $\text{Na}_{0.44}\text{MnO}_2$  and b)  $\text{Na}_{0.44}\text{Mn}_{0.95}\text{B}_{0.05}\text{O}_2$ ; HRTEM and FFT images of c)  $\text{Na}_{0.44}\text{MnO}_2$  and d)  $\text{Na}_{0.44}\text{Mn}_{0.95}\text{B}_{0.05}\text{O}_2$ ; e) TEM and EDS mapping images of the  $\text{Na}_{0.44}\text{Mn}_{0.95}\text{B}_{0.05}\text{O}_2$ .



**Figure 3.** Representative XPS patterns of  $\text{Na}_{0.44}\text{MnO}_2$  and  $\text{Na}_{0.44}\text{Mn}_{0.95}\text{B}_{0.05}\text{O}_2$ : a) full spectra, b) Mn 2p, c) O 1s, d) B 1s; e) relationship between electrical conductance and pressure, f) relationship between resistivity and pressure.

$\text{Na}_{0.44}\text{Mn}_{0.95}\text{B}_{0.05}\text{O}_2$  exhibit a characteristic Mn–O lattice vibration peak at  $660\text{ cm}^{-1}$ . Notably, compared with pristine  $\text{Na}_{0.44}\text{MnO}_2$ , the B-doped  $\text{Na}_{0.44}\text{MnO}_2$  sample displays a significantly enhanced peak intensity at  $583\text{ cm}^{-1}$ , which corresponds to the vibrational mode associated with oxygen vacancies.<sup>[22]</sup> This observation provides compelling evidence that B incorporation effectively increases the oxygen vacancy concentration, thereby modifying the local atomic environment and potentially influencing electrochemical performance.

The four-point probe results (Figure 3e,f) show that  $\text{Na}_{0.44}\text{Mn}_{0.95}\text{B}_{0.05}\text{O}_2$  has an average resistivity of  $20606.1\text{ }\Omega \cdot \text{cm}$  and a conductivity of  $5.47642 \times 10^{-5}\text{ S cm}^{-1}$ . In comparison,  $\text{Na}_{0.44}\text{MnO}_2$  exhibits an average resistivity of  $27966.1\text{ }\Omega \cdot \text{cm}$  and an average conductivity of  $4.2936 \times 10^{-5}\text{ S cm}^{-1}$ . The introduction

of B effectively reduces the resistivity of the cathode material and increases its conductivity, facilitating the rapid transfer of  $\text{Na}^+$  within the tunnel structure. However, as shown in Figure S6 (Supporting Information), the samples with higher B content,  $\text{Na}_{0.44}\text{Mn}_{0.9}\text{B}_{0.1}\text{O}_2$  and  $\text{Na}_{0.44}\text{Mn}_{0.8}\text{B}_{0.2}\text{O}_2$ , exhibit poorer conductivity. The increased B content leads to a higher proportion of the impurity phase  $\text{Mn}_2\text{O}_3$ , which results in greater resistance to  $\text{Na}^+$  conduction within the tunnel structure. Additionally, in Figure 3d, a B1s binding energy peak at 191.25 eV was detected in the core region of B, confirming the presence of B in  $\text{Na}_{0.44}\text{Mn}_{0.95}\text{B}_{0.05}\text{O}_2$ . Due to the low content of B and its relatively small photoionization cross-section as a light element, the resulting photoelectron signal is weak, making the fitting process challenging.

**Figure 4** shows the charge–discharge curves, rate capability, and cycling performance of  $\text{Na}_{0.44}\text{MnO}_2$  and  $\text{Na}_{0.44}\text{Mn}_{0.95}\text{B}_{0.05}\text{O}_2$ . As shown in Figure 4a,  $\text{Na}_{0.44}\text{MnO}_2$  and  $\text{Na}_{0.44}\text{Mn}_{0.95}\text{B}_{0.05}\text{O}_2$

provide the same capacities at a current density of 0.2C ( $1\text{C} = 121\text{ mA g}^{-1}$ ), both deliver a discharge capacity of  $112.2\text{ mAh g}^{-1}$ . As the current density increases, at current

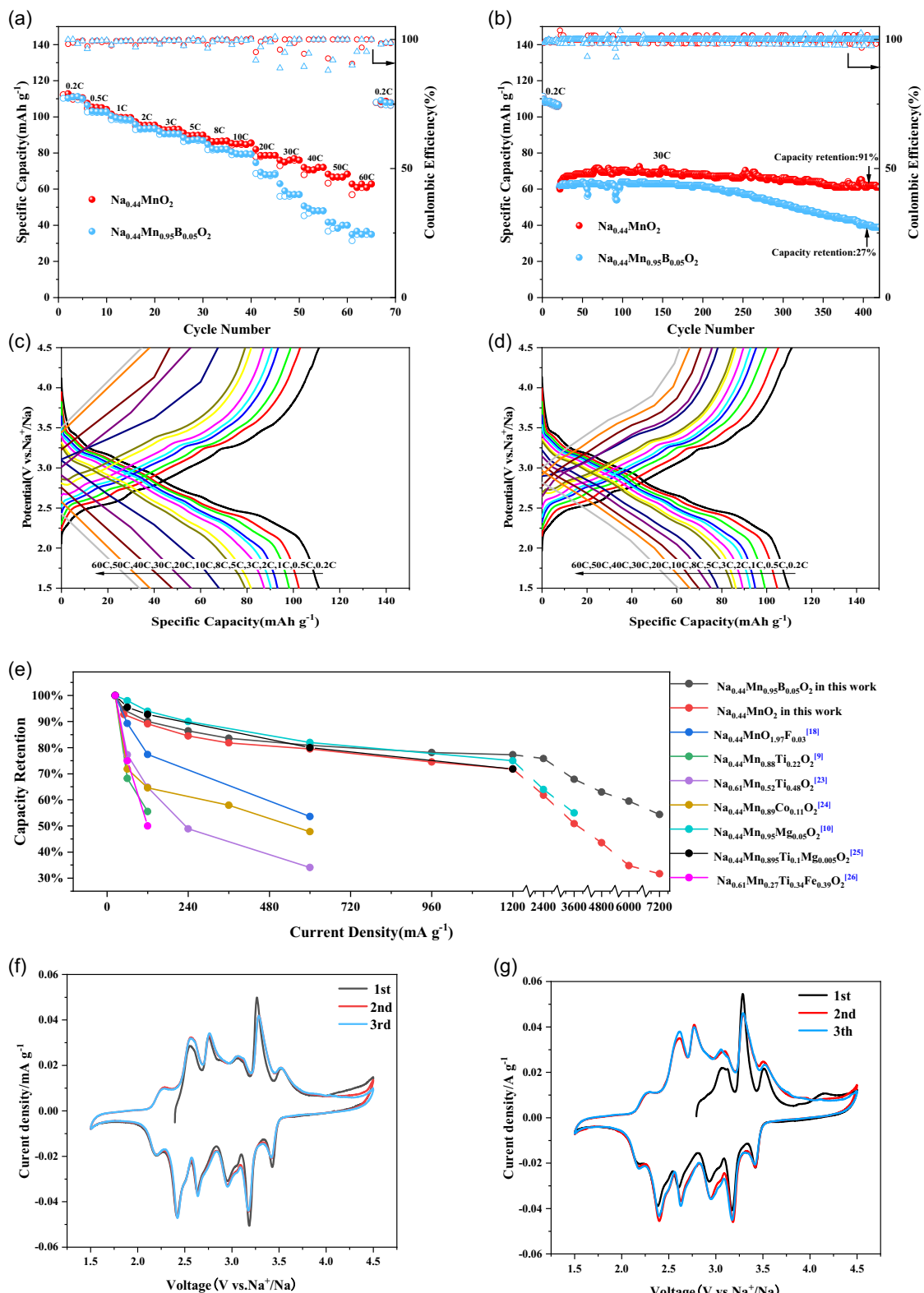


**Figure 4.** a) The rate properties of  $\text{Na}_{0.44}\text{MnO}_2$  and  $\text{Na}_{0.44}\text{Mn}_{0.95}\text{B}_{0.05}\text{O}_2$  cathodes. b) Comparison of cycling stability at a current of 30C after 20 cycles at 0.2C. c,d) Galvanostatic charge–discharge curves for  $\text{Na}_{0.44}\text{MnO}_2$  and  $\text{Na}_{0.44}\text{Mn}_{0.95}\text{B}_{0.05}\text{O}_2$  cathodes. e) Comparison of rate performance between the materials in this study and other materials. f) CV curves of  $\text{Na}_{0.44}\text{MnO}_2$  and g)  $\text{Na}_{0.44}\text{Mn}_{0.95}\text{B}_{0.05}\text{O}_2$ .

densities of 0.2, 0.5, 1, 2, 3, 5, 8, and 10 C, the capacities provided by NMO are 110.3, 102.6, 98.2, 90.4, 86.8, 82.1, and 79.3 mAh g<sup>-1</sup>, respectively, while those provided by Na<sub>0.44</sub>Mn<sub>0.95</sub>B<sub>0.05</sub>O<sub>2</sub> are 112.2, 104.7, 99.2, 95, 92.7, 89.5, 86.1, and 84.7 mAh g<sup>-1</sup>, respectively. As the current gradually increases to 60 C, Na<sub>0.44</sub>Mn<sub>0.95</sub>B<sub>0.05</sub>O<sub>2</sub> still maintains a capacity of 61.0 mAh g<sup>-1</sup>, which is 54% of that at 0.2 C, and after returning to 0.2 C, the capacity retention rate is above 95%. In contrast, the undoped material has a capacity of only 34.9 mAh g<sup>-1</sup> at 60 C, indicating a significant improvement in rate performance with B doping. Furthermore, the cycling performance of Na<sub>0.44</sub>MnO<sub>2</sub> and Na<sub>0.44</sub>Mn<sub>0.95</sub>B<sub>0.05</sub>O<sub>2</sub> is investigated and the results are shown in Figure 4b. After activation at 0.2 C for 20 cycles, the capacity retention rate of Na<sub>0.44</sub>Mn<sub>0.95</sub>B<sub>0.05</sub>O<sub>2</sub> after 400 cycles at 30 C is 91%, compared to only 27% capacity retention for Na<sub>0.44</sub>MnO<sub>2</sub>. Figure 4c,d show the corresponding charge/discharge curves at various C rates, displaying Na<sub>0.44</sub>Mn<sub>0.95</sub>B<sub>0.05</sub>O<sub>2</sub> still shows clear charging and discharging platforms under ultrahigh current densities. To further demonstrate the superiority of B doping, Figure 4e compares the capacity retention of the materials in this study with those reported in previous works under gradually increasing current densities.<sup>[9,10,18,23–26]</sup> The test current densities of cathode materials reported in the literature seldom reach 60 C. In contrast, the Na<sub>0.44</sub>Mn<sub>0.95</sub>B<sub>0.05</sub>O<sub>2</sub> synthesized in this study maintains a relatively high capacity even under high current densities. Obviously, B doping could significantly enhance the rate capability and cycle performance. However, as shown in Figure S6 (Supporting Information), although excessive B doping does not significantly affect the cyclic stability, it significantly affects the specific capacity. The capacity of Na<sub>0.44</sub>Mn<sub>0.9</sub>B<sub>0.1</sub>O<sub>2</sub> decreases to 84.2 mAh g<sup>-1</sup> at 0.2 C, and Na<sub>0.44</sub>Mn<sub>0.8</sub>B<sub>0.2</sub>O<sub>2</sub> provides a lower capacity of 70.9 mAh g<sup>-1</sup> at 0.2 C. This maybe due to excessive B doping causing an increased amount of the Mn<sub>2</sub>O<sub>3</sub> impurity phase, which reduces the electrochemical activity of Na<sub>0.44</sub>MnO<sub>2</sub> and decreases the reversible capacity. The CV curves of Na<sub>0.44</sub>MnO<sub>2</sub> and Na<sub>0.44</sub>Mn<sub>0.95</sub>B<sub>0.05</sub>O<sub>2</sub> at a scan rate of 0.1 mV s<sup>-1</sup> are shown in Figure 4f,g. The CV curves exhibit at least six pairs of redox peaks, which are consistent with previous reports of multiple phase transitions in Na<sub>0.44</sub>MnO<sub>2</sub> during

electrochemical reactions. The incorporation of B does not significantly alter the curves.

The sodium ion diffusion coefficients of unmodified Na<sub>0.44</sub>MnO<sub>2</sub> and Na<sub>0.44</sub>Mn<sub>0.95</sub>B<sub>0.05</sub>O<sub>2</sub> were determined using galvanostatic intermittent titration technique (GITT) (Figure 5a), with specific calculation formulas provided in the supporting information. Both materials were tested at a current density of 0.01 C after 5 activation cycles. The GITT curve of Na<sub>0.44</sub>Mn<sub>0.95</sub>B<sub>0.05</sub>O<sub>2</sub> is shown in the figure, and the calculated sodium ion diffusion coefficients (D<sub>Na<sup>+</sup></sub>) based on the diffusion curves of Na<sub>0.44</sub>MnO<sub>2</sub> and Na<sub>0.44</sub>Mn<sub>0.95</sub>B<sub>0.05</sub>O<sub>2</sub> are presented in the figure as well. The diffusion coefficient D<sub>Na<sup>+</sup></sub> of NMO fluctuates within the range of 4.0 × 10<sup>-12</sup> to 3.1 × 10<sup>-10</sup> cm<sup>2</sup> s<sup>-1</sup>, with an average of 7.7 × 10<sup>-11</sup> cm<sup>2</sup> s<sup>-1</sup>. After modification, the diffusion coefficient of Na<sub>0.44</sub>Mn<sub>0.95</sub>B<sub>0.05</sub>O<sub>2</sub> fluctuates within the range of 8.2 × 10<sup>-10</sup> to 4.9 × 10<sup>-8</sup> cm<sup>2</sup> s<sup>-1</sup>, with an average of 8.8 × 10<sup>-9</sup> cm<sup>2</sup> s<sup>-1</sup>, which is two orders of magnitude higher. These results demonstrate that the addition of B can increase the diffusion rate of Na ions.

Further investigation of the influence of B on tunnel-type oxides was conducted through electrochemical impedance spectroscopy (EIS), and detailed Nyquist plots of Na<sub>0.44</sub>MnO<sub>2</sub> and Na<sub>0.44</sub>Mn<sub>0.95</sub>B<sub>0.05</sub>O<sub>2</sub> are shown in Figure 5b. A clear low peak is observed in the high-frequency region, attributed to charge transfer resistance (R<sub>ct</sub>), while the sloping line in the low-frequency region represents Warburg impedance. Specific impedance values were obtained through Zview fitting and the results are listed in Table S4 (Supporting Information). The R<sub>ct</sub> of Na<sub>0.44</sub>MnO<sub>2</sub> is 195.3 Ω, whereas the R<sub>ct</sub> of Na<sub>0.44</sub>Mn<sub>0.95</sub>B<sub>0.05</sub>O<sub>2</sub> decreases to 108.7 Ω. The smaller R<sub>ct</sub> means a smaller resistance during Na ion transfer, allowing for higher capacity at high current densities.

Building on the excellent performance of Na<sub>0.44</sub>Mn<sub>0.95</sub>B<sub>0.05</sub>O<sub>2</sub> in half-cells, we assembled a sodium-ion full cell using Na<sub>0.44</sub>Mn<sub>0.95</sub>B<sub>0.05</sub>O<sub>2</sub> as the cathode and commercial hard carbon as the anode to evaluate its practicality in energy storage applications. Considering the limited sodium content in Na<sub>0.44</sub>MnO<sub>2</sub> and the low initial Coulombic efficiency of hard carbon, pre-sodiation was performed on both the cathode and anode materials

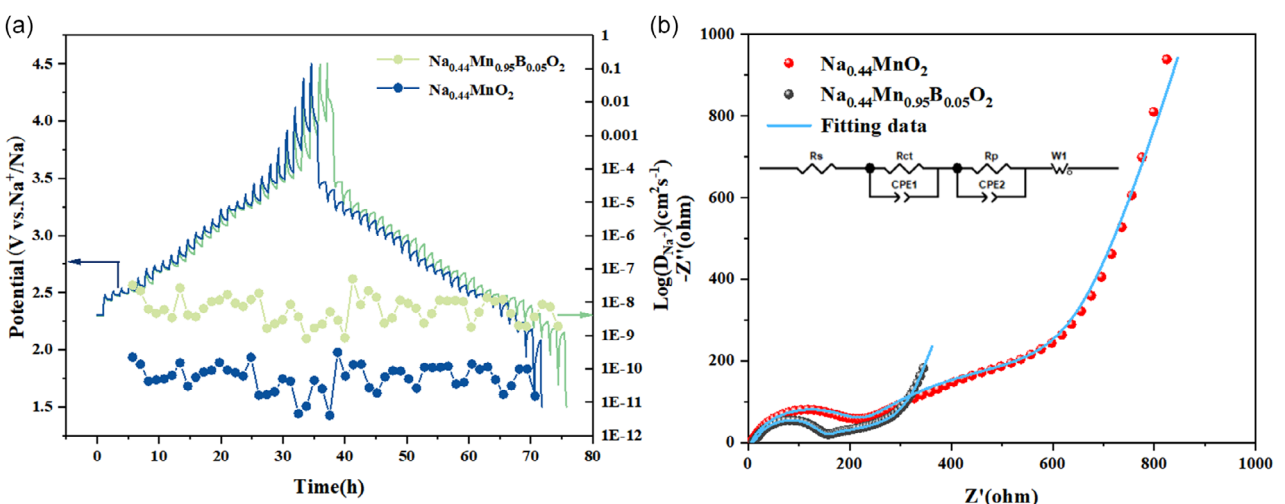


**Figure 5.** a) GITT and corresponding Na<sup>+</sup> diffusion coefficients of Na<sub>0.44</sub>MnO<sub>2</sub> and Na<sub>0.44</sub>Mn<sub>0.95</sub>B<sub>0.05</sub>O<sub>2</sub>. b) Nyquist plots in the initial state of Na<sub>0.44</sub>MnO<sub>2</sub> and Na<sub>0.44</sub>Mn<sub>0.95</sub>B<sub>0.05</sub>O<sub>2</sub>.

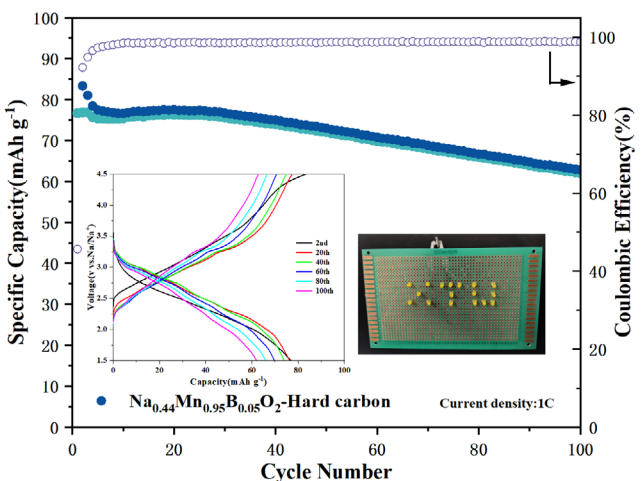


**Figure 6.** Cycling performance at 1 C and Galvanostatic charge–discharge curves of  $\text{Na}_{0.44}\text{Mn}_{0.95}\text{B}_{0.05}\text{O}_2/\text{Hard carbon}$ .

prior to assembling the full cell. This step aimed to minimize irreversible capacity loss and enhance cycling stability.

Figure 6 presents the cycling performance of the full cell at 1 C. The specific capacity of the cell was evaluated based on the mass of the cathode material. Operating within a voltage window of 1.5–4.5 V, the full cell retained 81.9% of its capacity after 100 cycles, demonstrating excellent cycling stability and stable coulombic efficiency. These outstanding electrochemical properties confirm the promising potential of  $\text{Na}_{0.44}\text{Mn}_{0.95}\text{B}_{0.05}\text{O}_2$  for practical applications in sodium-ion batteries.

### 3. Conclusion

In summary, the effect of B doping on the sodium storage performance of tunnel-type  $\text{Na}_{0.44}\text{MnO}_2$  was systematically investigated. B doping promotes the formation of oxygen vacancies, resulting in better electronic conductivity of  $\text{Na}_{0.44}\text{Mn}_{0.95}\text{B}_{0.05}\text{O}_2$ . Besides, B doping expands the cell volume and promotes  $\text{Na}^+$  insertion/deinsertion. Thus, compared to the undoped  $\text{Na}_{0.44}\text{MnO}_2$ , the appropriate amount of B doping could enhance the electrochemical performance, especially the rate performance.  $\text{Na}_{0.44}\text{Mn}_{0.95}\text{B}_{0.05}\text{O}_2$  delivers a reversible capacity of  $61 \text{ mA g}^{-1}$  at a high current density of 60 C and maintains a capacity retention of 91% after 400 cycles at 30 C, which are much higher than the undoped sample. The results from GITT and EIS demonstrate a significant increase in  $\text{Na}^+$  diffusion coefficient and reduction in charge transfer resistance after B doping. This work provides better insights for the improvement of future manganese-based positive electrode materials.

### 4. Experimental Section

#### Synthesis of Cathode Materials

$\text{Na}_{0.44}\text{Mn}_{1-x}\text{B}_x\text{O}_2$  ( $x = 0.05, 0.1$  and  $0.2$ ) cathode materials were prepared using sodium acetate, manganese acetate, and boric acid as raw materials, with citric acid as a chelating agent, via the sol-gel method.  $\text{CH}_3\text{COONa}$ ,  $\text{Mn}(\text{CH}_3\text{COO})_2 \cdot 4\text{H}_2\text{O}$ , and  $\text{H}_3\text{BO}_3$  were added

to 100 mL of deionized water according to the stoichiometric ratio to form solution A. Citric acid in an amount equal to twice the molar quantity of transition metals was dissolved in 100 mL of deionized water to form solution B. Solution B was slowly added dropwise to solution A, and the mixture was stirred at  $80^\circ\text{C}$  until complete evaporation of water. The resulting gel was dried overnight at  $120^\circ\text{C}$  in an oven, then ground repeatedly using a agate mortar. The dried mixture was pre-calcined at  $400^\circ\text{C}$  in a muffle furnace to remove citric acid, followed by thorough grinding to ensure homogeneity. Finally, the mixture was calcined at  $900^\circ\text{C}$  in air with a heating rate of  $3^\circ\text{C min}^{-1}$  for 12 h to obtain  $\text{Na}_{0.44}\text{Mn}_{1-x}\text{B}_x\text{O}_2$ . Undoped  $\text{Na}_{0.44}\text{MnO}_2$  was prepared using a similar method, but  $\text{H}_3\text{BO}_3$  was not added during the synthesis process.

#### Materials Characterization

The crystal structure of the samples was studied using X-ray powder diffraction (XRD), with diffraction patterns recorded in the  $2\theta$  range of  $5^\circ$ – $60^\circ$ , and the Rietveld refinement was performed with the GSASII software. Raman spectroscopy (Renishaw inVia RM200) and FTIR (FTIR, ALPHA) was used for structural characterization. The surface morphology and internal crystal structure of the samples were investigated using scanning electron microscopy (SEM, JEOL SM-71480) and transmission electron microscopy (TEM, JEOL JEM-100CX), and the distribution and composition of elements in the samples were studied using energy-dispersive X-ray spectroscopy (EDS). The elemental valence states of the samples were analyzed using X-ray photoelectron spectroscopy (XPS, PHI 5000 Versa Probe).

#### Electrochemical Testing and Analysis

70% as-prepared cathode material, 20% acetylene black (Super P, Canrud), and 10% PVDF (Canrud) binder were mixed to form a slurry in N-methylpyrrolidinone (NMP, Aladdin) solvent. The slurry was evenly coated on aluminum foil current collectors using a coater, and dried in a vacuum oven at  $80^\circ\text{C}$  for 12 h to obtain the cathode sheet. The dried cathode was punched into disks with a diameter of 10 mm, and the active material loading in the positive electrode was  $\approx 2.0 \text{ mg cm}^{-2}$ . The prepared positive electrode material, metallic sodium as the negative electrode, and 1 M  $\text{NaClO}_4$  dissolved in ethylene carbonate and diethyl carbonate (EC DEC = 1:1) with 5 wt% fluoroethylene carbonate (FEC) as the electrolyte were assembled with glass fiber (Whatman, GF/D) as the separator to form 2032 coin cells for a series of electrochemical tests. All charge/discharge tests and GITT measurements were conducted on a Neware BT3008 W battery tester (Shenzhen, China), with a voltage range of 1.5–4.5 V (vs  $\text{Na}^+/\text{Na}$ ). Cyclic voltammetry (CV) and electrochemical impedance spectroscopy (EIS) experiments were performed on a CHI 660 E electrochemical workstation (Chenhua, Shanghai, China). The electrical conductance and resistivity were analyzed using four-point probe with automatic powder resistivity tester (ST2742B).

#### Acknowledgements

W.D. and Z.Y. contributed equally to this work. This work was supported by the National Natural Science Foundation of China (grant no. 52372230) and Research Foundation of Education Bureau of Hunan Province, China (grant no. 23B0149).

#### Conflict of Interest

The authors declare no conflict of interest.

## Data Availability Statement

The data that support the findings of this study are available from the corresponding author upon reasonable request.

**Keywords:** B doping · high-rate ·  $\text{Na}_{0.44}\text{MnO}_2$  · sodium manganese oxide

- [1] J. M. Tarascon, M. Armand, *Nature* **2001**, *414*, 359.
- [2] M. S. Whittingham, *Chem. Rev.* **2004**, *104*, 4271.
- [3] P. F. Wang, Y. You, Y. X. Yin, Y. G. Guo, *Adv. Energy Mater.* **2018**, *8*, 1701912.
- [4] J. Dai, J. Jing, J. P. Yang, W. Zhang, S. X. Liu, Q. F. Wang, J.-X. Wen, H. Hu, H.-F. Li, L. Liu, *Rare Met.* **2023**, *42*, 3387.
- [5] J. Y. Hwang, S. T. Myung, Y. K. Sun, *Chem. Soc. Rev.* **2017**, *46*, 3529.
- [6] M. Ren, H. Fang, C. Wang, H. Li, F. Li, *Energy Fuels* **2020**, *34*, 13412.
- [7] M. S. Chae, Y. Elias, D. Aurbach, *ChemElectroChem* **2021**, *8*, 798.
- [8] A. N. Singh, M. Islam, A. Meena, M. Faizan, D. Han, C. Bathula, A. Hajibabaei, R. Anand, K.-W. Nam, *Adv. Funct. Mater.* **2023**, *33*, 2304617.
- [9] P. Zhan, K. Jiao, J. Wang, Z. Hu, R. Ma, H. Zhu, S. Jiao, *J. Electrochem. Soc.* **2015**, *162*, A2296.
- [10] X. L. Li, J. Bao, Y. F. Li, D. Chen, C. Ma, Q. Q. Qiu, X.-Y. Yue, Q.-C. Wang, Y.-N. Zhou, *Adv. Sci.* **2021**, *8*, 2004448.
- [11] J. Guan, S. Zhou, J. Zhou, F. Wu, X. Shi, J. Xu, P. Wu, Y. Zhou, P. He, Y. Tang, H. Zhou, *ACS Appl. Mater. Interfaces* **2024**, *16*, 20559.
- [12] C. Liu, K. Chen, H. Xiong, A. Zhao, H. Zhang, Q. Li, X. Ai, H. Yang, Y. Fang, Y. Cao, *eScience* **2024**, *4*, 100186.
- [13] E. Oz, S. Demirel, S. Altin, A. Bayri, S. Avci, *Ceram. Int.* **2016**, *42*, 17059.
- [14] H. Kim, D. J. Kim, D. H. Seo, M. S. Yeom, K. Kang, D. K. Kim, Y. Jung, *Chem. Mater.* **2012**, *24*, 1205.
- [15] J. Zhao, X. Zhang, Q. Zhao, L. Wang, Y. Wang, *Chem. Phys.* **2020**, *529*, 110582.
- [16] S. Demirel, E. Oz, E. Altin, S. Altin, A. Bayri, P. Kaya, S. Turan, S. Avci, *Mater. Charact.* **2015**, *105*, 104.
- [17] K. Chu, Y. P. Liu, Y.-H. Cheng, Q.-Q. Li, *J. Mater. Chem. A* **2020**, *8*, 5200.
- [18] W. J. Shi, Y.-W. Yan, C. Chi, X.-T. Ma, D. Zhang, S.-D. Xu, L. Chen, X.-M. Wang, S.-B. Liu, *J. Power Sources* **2019**, *427*, 129.
- [19] K. Jiang, S. Guo, W. K. Pang, X. Zhang, T. Fang, S.-F. Wang, F. Wang, X. Zhang, P. He, H. Zhou, *Nano Res.* **2021**, *14*, 4100.
- [20] C. H. Rim, C. H. Jang, K.-H. Kim, C. Ryu, C. J. Yu, *Phys. Phys. Chem. Chem. Phys.* **2022**, *24*, 22736.
- [21] X. Zhao, B. Wen, Q. Dong, P. Wang, X. Lyu, *Int. J. Hydrogen Energy* **2025**, *105*, 556.
- [22] P. Gong, J. Xie, D. Fang, F. He, F. Li, K. Qi, *Mater. Res. Express* **2017**, *4*, 115036.
- [23] S. H. Guo, H. Yu, D. Liu, W. Tian, X. Liu, N. Hanada, M. Ishida, H. Zhou, *Chem. Commun.* **2014**, *50*, 7998.
- [24] Y. T. Zhou, X. Sun, B. K. Zou, J. Y. Liao, Z. Y. Wen, C. H. Chen, *Electrochim. Acta* **2014**, *213*, 496.
- [25] H. Zhonge, J. Yuxuan, J. Wang, L. Yuhua, Z. Wenqing, J. Hongyuqi, S. Yongqiang, W. Xianwen, X. Yanhong, *J. Solid State Chem.* **2024**, *329*, 124415.
- [26] S. Xu, Y. Wang, L. Ben, Y. Lyu, N. Song, Z. Yang, Y. Li, L. Mu, H.-T. Yang, L. Gu, Y.-S. Hu, H. Li, Z.-H. Cheng, L. Chen, X. Huang, *Adv. Energy Mater.* **2015**, *5*, 1501156.

Manuscript received: January 14, 2025

Revised manuscript received: March 18, 2025

Version of record online: March 20, 2025